JBC RESEARCH ARTICLE

Cyclosporine A sterically inhibits statin transport by solute carrier OATP1B1

Received for publication, August 8, 2024, and in revised form, March 24, 2025 Published, Papers in Press, April 6, 2025,
https://doi.org/10.1016/j.jbc.2025.108484

Min Woo Sung[1], Kuan Hu[1], Lea M. Hurlimann[2], Joshua A. Lees[1], Kimberly F. Fennell[1], Mark A. West[3], Chester Costales[3], Amilcar David Rodrigues[3], Iwan Zimmermann[2], Roger J. P. Dawson[2], Shenping Liu[1,*], and Seungil Han[1,*]

From the [1]Discovery Sciences, Discovery & Early Development, Pfizer Inc, Groton, Connecticut, USA; [2]Linkster Therapeutics AG, Zurich, Switzerland; [3]Pharmacokinetics, Dynamics, and Metabolism, Discovery & Early Development, Pfizer Inc, Groton, Connecticut, USA

Reviewed by members of the JBC Editorial Board. Edited by Mike Shipston

Members of the Organic Anion Transporter Polypeptides (OATP) are integral membrane proteins responsible for facilitating the transport of organic anions across the cell membrane. OATP1B1 (SLCO1B1), the prototypic OATP family member, is the most abundant uptake transporter in the liver and a key mediator of the hepatic uptake and clearance of numerous endogenous and xenobiotic compounds. It serves as a locus of important drug-drug interactions, such as those between statins and cyclosporine A, and carries the potential to enable liver-targeting therapeutics. In this study, we report cryo-EM structures of OATP1B1 and its complexes with one of its statin substrates, atorvastatin, and an inhibitor, cyclosporine A. This structural analysis has yielded insights into the mechanisms underlying the OATP1B1-mediated transport of statins and the inhibitory effect of cyclosporine A. These findings contribute to a better understanding of the molecular processes involved in drug transport and offer potential avenues for the development of targeted medications for liver-related conditions.

Transporter-mediated hepatic uptake and clearance pathways influence the efficacy and safety of drugs by modulating their absorption, distribution, metabolism, and elimination (ADME) properties. Dysfunction of these pathways, caused by genetic polymorphism or by pharmacological inhibition, is associated with variations in patient responses to drugs. Human Organic Anion Transporting Polypeptides (OATPs), which comprise six sub-families of 12-transmembrane transporter glycoproteins (1–3), are encoded by genes of the Solute Carrier Organic Anion (*SLCO*) family (2, 4). Their substrates, which include bile acids, bilirubin, steroid hormone conjugates, thyroid hormones, prostaglandins, toxins, and many clinically used drugs, tend to be large (>300 Da), amphipathic, and negatively charged (5), while substrates of the related Organic Anion Transporter (OAT) family are similar but in general tend to be smaller and more hydrophilic (6) (for a fuller analysis of the molecular determinants of OAT vs. OATP substrates, please refer to (7)). OATP family members OATP1B1 and OATP1B3 are highly expressed in the liver and function on the basolateral plasma membrane of hepatocytes (8–11). As such, they play important roles in hepatic uptake and clearance of both natural and xenobiotic substrates, which has implicated them in numerous drug-drug interactions (DDIs). In recognition of this association, the latest guidance documents for pharmaceutical companies published by the United States Food and Drug Administration (FDA) and the European Medical Agency (EMA) recommend screening drug candidates for interactions with both OATP1B1 and OATP1B3 (12, 13).

OATP1B1 is a major hepatic transporter for many pharmacological agents, of which HMG-CoA reductase inhibitors ("statins"), which are also substrates for transporters of the related OAT family (14), are among the best-studied examples. *In vitro* and *in vivo* studies have established that drugs with inhibitory activity against OATP1B1 can cause clinically relevant DDIs. For example, the immunosuppressant cyclosporine A, which is commonly used in the prevention of organ transplant rejection and in the treatment of some autoimmune diseases, inhibits OATP1B1-mediated transport of statins, such as rosuvastatin and atorvastatin, reducing their elimination and markedly increasing their concentrations in plasma (15, 16). Cyclosporine-mediated elevation of serum statin levels can lead to clinical complications, with severe cases linked to statin-induced rhabdomyolysis (17).

To elucidate the molecular basis of such DDIs, a structural understanding of transporters with their substrates and inhibitors is critical. Cryo-electron microscopy (cryo-EM) has proven to be a powerful tool in recent years for the determination of many solute carriers' mechanisms of action (18), and indeed two publications have recently reported structures of OATP family members, providing useful insights into ligand binding and clues to the structural basis of transport. One study (19) revealed the inward-facing structures of OATP1B1 (bound to substrate estrone-3-sulfate, E1S) and OATP1B3, enabled by Fab fragments, and the other (20) reported multiple structures of OATP1B1, in its apo form and in complexes with

* For correspondence: Shenping Liu, shenping.liu@pfizer.com; Seungil Han, seungil.han@pfizer.com.

substrates bilirubin and E1S, inhibitor simeprevir, and a fluorophore (2′7′-dichlorofluorescein; DCF) used in transport assays. No structures of OATP1B1 with cyclosporine A or statins, however, have been reported.

In this study, we have used structural characterization of OATP1B1 by cryo-EM, facilitated by a newly developed synthetic nanobody ("sybody") to better understand the binding modes and transport mechanisms underlying statin transport, with a focus on atorvastatin as a representative example. Additionally, we provide the first structure of OATP1B1 bound to cyclosporine A, shedding light on the mechanistic basis of its sterically driven transport inhibition. These findings provide insights into the mechanism of a well-studied and clinically relevant DDI.

Results

A novel synthetic nanobody assists high-resolution structural characterization of OATP1B1 in its outward-open state

To understand the molecular basis of statin transport by OATP1B1 and its inhibition by cyclosporine A, we undertook structural analysis of the transporter by cryo-EM. These efforts were initially hampered by a combination of the protein's intrinsic conformational flexibility and a particle orientation bias, which introduced anisotropy in the resulting maps and presented challenges to their interpretation. Therefore, to enable a high-resolution structural solution, we performed screening to identify a synthetic nanobody against OATP1B1, as described previously (21), in the hope of facilitating the capture of additional particle views while potentially reducing the transporter's conformational flexibility. From these efforts, a sybody was identified, which we term sybody 5 (hereafter Sb5), that binds to OATP1B1 in both its apo and cyclosporine A-bound forms with similar affinities (12.9 nM and 30.5 nM, respectively; Fig. 1*A*). Importantly, Sb5 does not inhibit OATP1B1 transport activity, as measured by uptake of atorvastatin or rosuvastatin, in cells over-expressing OATP1B1 (Fig. S1).

Cryo-EM analysis of the OATP1B1-Sb5 complex yielded a high-resolution reconstruction of the transporter in its outward-facing state (Fig. 1*B*). While both inward- and outward-facing conformations were identified in the particle population in the absence of Sb5, other intermediate conformations could not be resolved to high resolution when Sb5 is present. As noted in other recently published structures (19, 20), OATP1B1 conforms to the major facilitator subfamily (MFS) clan fold, with 6 transmembrane helices forming each of two bundles that together form the "rocking switch" that accomplishes transport. Extracellular loops between the transmembrane (TM) helices form domains extending from the N-lobe (formed by residues 117–168, 233–256) and the C-lobe (formed by residues 431–527, 599–617)), and the C-lobe extracellular Kazal-like domain is stabilized by five disulfide bridges, formed by cysteine pairs C489/C504, C459/C506, C465/C485, C474/C524, and C599/C613. An additional disulfide bond between C142-C463 bridges between extracellular loops of the N and C lobes, although the bulk of the connecting loop (N-lariat) is disordered in the structure.

The Sb5 epitope is located in the N-terminal helical bundle of OATP1B1, spanning extracellular loops 2 and 3 and portions of TM3 and TM4. (Fig. 1*C*). This epitope is adjacent to that of the recently reported Fab 18, which enabled the determination of the inward-open-biased structure of E1S-bound OATP1B1, but the respective epitopes overlap by only a single residue, Y239 (19). Of note, R103 of Sb5 participates in a hydrogen bond with H115 of OATP1B1 (Fig. 1, *C* and *D*), which corresponds to a histidine residue of OATP1A1 identified as the locus of pH-sensitive transport (22). Conceivably, this direct contact between Sb5 and H115 could play a role in altering or abolishing the pH sensitivity of OATP1B1, but its role remains unclear. Based on our biochemical data, Sb5 does not impair the ability of OATP1B1 to transport substrates and thus does not prevent the transition to the inward-facing conformation. However, when the structure of inward-facing OATP1B1 was determined from the same dataset used for the Sb5-bound outward-facing structure, no clear evidence of Sb5 density was observed. Notably, of the OATP1B1 residues participating in the Sb5 epitope, all but Y169 are conserved in OATP1B3.

The conformation of Sb5-bound OATP1B1 is similar to that of other published outward-facing structures (8hnb (apo), 8hnc (bilirubin), 8hnh (simeprevir), 8k6l (DCF)) with a root-mean-square deviation (rmsd) of less than 1 Å (Fig. S2*A*). Minor differences are largely attributable to intrinsic flexibility in the C-lobe extracellular domain (20). In a notable departure, however, residues 371 to 379 of OATP1B1 are disordered in our map, whereas they form the N-terminal segment of TM helix 8 in both the liganded and unliganded published structures (Fig. S2*B*). This segment resides at the extracellular periphery of the cavity, near the interface between lobes, though it forms no contact with its nearest N-lobe neighbor, TM4, in any of the structures. Because these residues occur in the C-lobe, there is no clear structural evidence linking this discrepancy to the binding of Sb5, and its underlying cause remains unclear, but it is possible that structural flexibility in this helix plays a role in conformational transitions or ligand binding, since it neighbors the major ligand binding pocket.

In its outward-facing conformation, the substrate-binding cavity of OATP1B1 is lined primarily by hydrophobic residues, with a wide opening toward the extracellular side of the membrane that gradually constricts toward a cluster of four residues (L193, L209, V556, and L572) (Fig. S3*A*), which acts as a gate to prevent access to the intracellular side. Between the two helical bundles, the outward-facing conformation forms a V-shaped opening through which the cavity is exposed to the membrane, occupied by unmodeled elongated densities in the map consistent with lipid molecules (Fig. S3*B*). This feature may allow OATP1B1 access to substrates fully or partially inserted in the membrane. A stabilizing salt bridge between D198 and K568 connects the two lobes in this conformation. Conversely, R57 and K361 have been identified as critical residues for transport (23), and these residues appear on opposite sides of the extracellular opening of the outward-facing receptor (Fig. S3*C*). In the inward-facing conformation, they each form a salt bridge with an acidic residue on the

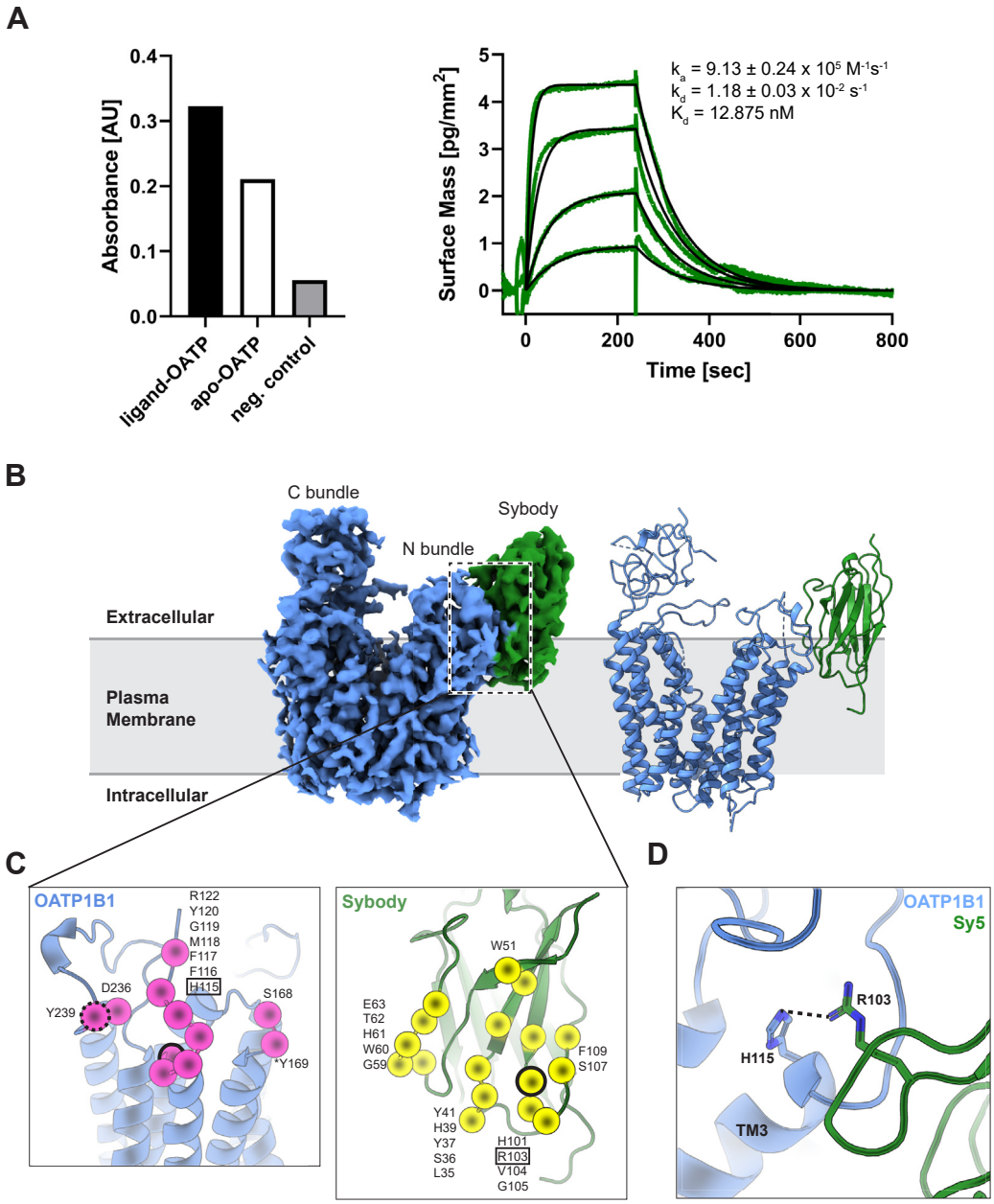

Figure 1. Sybody Selection and Characterization and Structure of apo-OATP1B1 with Sb5. *A*, Sybody 5 binding to apo and cyclosporine A-bound OATP1B1 was characterized by ELISA (*left panel*). Kinetic parameters for Sb5 binding to apo-OATP1B1 were determined using grating-coupled interferometry (GCI) (*right panel*). *B*, cryo-EM map volume of outward-facing apo-OATP1B1-Sb5 complex and ribbon representation of coordinates, colored by subunit, as indicated. *C*, residues participating in OATP-Sb5. *Left panel*, epitope residues are highlighted as magenta spheres with associated residue numbers indicated. Residue bordered by *dotted line* overlaps with the epitope of Fab 18 (Ciuta *et al.*, 2023). Y169, indicated by an *asterisk*, is a histidine in OATP1B3. *Right panel*, paratope residues are highlighted as *yellow spheres* with residue numbers indicated. *Solid borders* indicate residues highlighted in Figure 1*D*. *D*, R103 of Sb5 participates in a hydrogen bond with H115 of OATP1B1, indicated by a *dotted line*.

opposite lobe (R57 with E364; K361 with E56), forming a similar gate blocking access to the extracellular side and stabilizing the inward-open state for substrate release (19).

Basic residues, K41 and R580, are found at the base of an otherwise hydrophobic substrate-binding cavity, which is consistent with its transport of anionic substrates and contrasts with members of the related organic cation transporter (OCT) family (24), whose interiors are lined by acidic residues to accommodate cationic substrates. Additionally, a ladder of alternating acidic and basic residues runs up the N-terminal helical bundle toward the extracellular surface, comprising K49, D70, R181, and E74, making the N-terminal side of the cavity relatively hydrophilic (Fig. S3*D*). The C-terminal side of the cavity is primarily hydrophobic, although R580 forms a potential salt bridge with E185 of the N-terminal bundle.

Atorvastatin binding to the OATP1B1 substrate pocket is plastic

Atorvastatin is an HMG-CoA reductase inhibitor (statin) used to reduce serum low-density lipoprotein (LDL)

cholesterol. Atorvastatin, like other statins, is an amphipathic acid and a non-inhibitory transport substrate for OATP1B1. To elucidate the mechanism of atorvastatin transport by OATP1B1, we determined its structure bound to Sb5 in the presence of atorvastatin at 3.2 Å resolution (Fig. 2*A*). Similar to our observations in the apo state, the transporter adopted both inward- and outward-facing conformations on the grid, but only the outward-facing conformation could be resolved with high resolution.

Map density for atorvastatin in the OATP1B1 ligand-binding pocket is clear, but not well-defined, likely reflecting partial occupancy or a heterogeneous pose, which precluded a detailed analysis of specific ligand-protein interactions (Fig. 2*A*, inset). Ciuta and colleagues, who reported the structure of inward-facing OATP1B1 bound to E1S, used predictive tools to identify the possible dispositions of both atorvastatin and rosuvastatin within the substrate-binding cavity, predicting that their acidic moieties protrude into the hydrophilic so-called "minor pocket", much like the sulfate group of E1S (19, 20). Our best fitting of atorvastatin to the cryo-EM map density suggests that atorvastatin lies entirely within the major pocket described previously (Fig. 2*B*, shown in orange), more in agreement with known structures of OATP1B1 bound to simeprevir and DCF. Its acidic moiety protrudes toward a basic patch near the base of the pocket lined by K41 and R580, rather than into the minor pocket occupied by the sulfate group of E1S. The three aromatic substituents extending from atorvastatin's central pyrrole ring

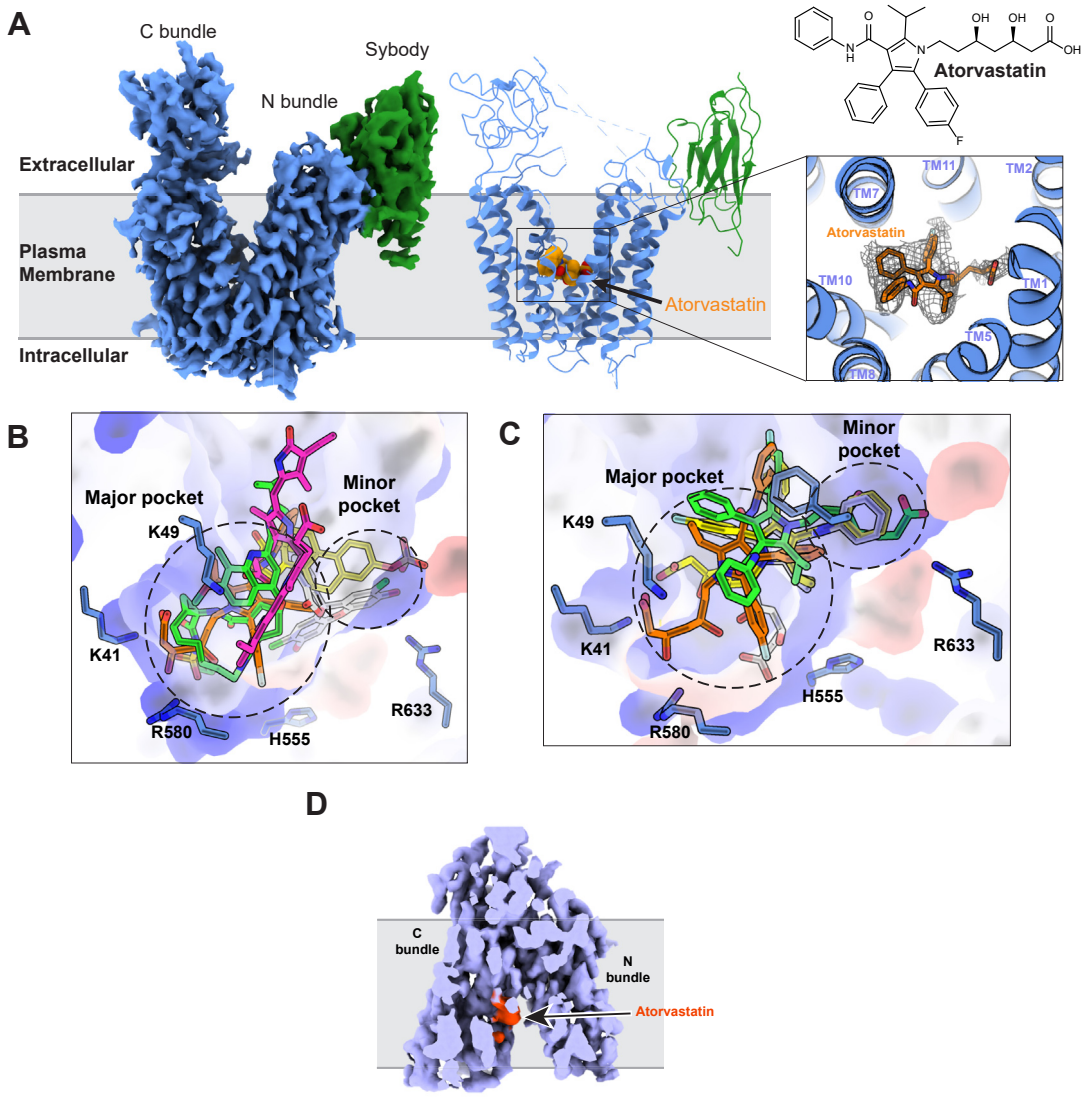

Figure 2. Structure of atorvastatin-bound OATP1B1 with Sb5. *A*, cryo-EM map volume of outward-facing OATP1B1-Sb5 complex bound to atorvastatin and ribbon representation of coordinates, colored by subunit, as indicated. The inset shows the atorvastatin binding site with its corresponding map density, contoured at 3.0σ. *B*, Ligand-bound structures of OATP1B1 (PDB 8K61 (DCF; *white*), PDB 8HNH (simeprevir; *green*), PDB 8HND (estrone-3-sulfate; *yellow*), PDB 8HNC (bilirubin; *magenta*)) are aligned with the atorvastatin-bound structure (*orange*). The transparent surface represents the APBS electrostatics surface calculation for atorvastatin-bound OATP1B1, with the major and minor pockets indicated. *C*, comparison of outward-open atorvastatin binding mode with Autodock Vina predictions. The atorvastatin molecule built into the cryo-EM density is colored in *orange*, with additional predicted binding poses superimposed in *white*, *green*, and *yellow*. *D*, low-resolution cryo-EM map of Sb5-free inward-open OATP1B1 bound to atorvastatin. Non-protein density attributed to atorvastatin is colored in *magenta*.

likely form favorable interactions with the hydrophobic surface comprising primarily residues on the C-lobe side of the pocket, particularly aromatics, including Y352, F356, and F386. This positioning of the ligand, therefore, would represent a reorientation of nearly 180° from the prediction, forming a distinct set of polar interactions on the opposite lobe. To further build confidence in this pose, we used our outward-facing OATP1B1 coordinates with Autodock Vina (25, 26) to predict binding modes for atorvastatin, but used an expanded pocket which included both the described minor and major pockets. While this prediction did yield a pose that broadly agrees with our interpretation of the map, it also yielded additional poses, including one similar to previous modeling (19), which makes use of the minor pocket, with similar confidence (Fig. 2*C*). We conclude that atorvastatin may bind the pocket in any one of multiple modes, potentially making different sets of favorable interactions. The ligand's orientational and conformational heterogeneity would also explain its poorly defined map density.

Atorvastatin's acidic moiety in its various predicted poses resides near different basic or hydrophilic patches located around the pocket comprising residues K41, K49, H555, and R580. Residue H555 is of particular interest, as OATP1B3 contains a phenylalanine in this position that has been shown to have a role in the transport of epigallocatechin gallate (EGCG). An F555H mutation significantly reduced EGCG transport by OATP1B3 (27). Conversely, cholecystokinin-8 (an OATP1B1-specific substrate) uptake by OATP1B1 was abolished in an H555 F variant (28), suggesting this position is important for the transport of some substrates by both OATP1B1 and OATP1B3. To probe the importance of the basic residues lining the major and minor pockets for substrate transport, we measured the transport of both atorvastatin and rosuvastatin by OATP1B1 mutants in which key residues were replaced with alanine (Fig. S4*A*). Their relative transport rates suggested that mutation of K41, K49, or R580 causes a significant reduction in transport compared to the wild-type transporter, which would accord with our cryo-EM modeling suggesting that these residues are needed to accommodate atorvastatin's acidic moiety. In contrast, mutation of R633, which resides in the minor pocket, contacts the sulfate of E1S, and was predicted to possibly contact atorvastatin's acid group, had no discernable effect on transport of either substrate. H555 was mutated to either alanine or phenylalanine, the latter to mimic the residue natively found in OATP1B3. Interestingly, while both mutations reduced the transport of atorvastatin, only the OATP1B3-mimicking phenylalanine reduced the transport of rosuvastatin. It must be noted, however, that our efforts at quantitation of these mutants' relative total or cell surface expression levels compared to wild-type encountered significant challenges, and we were ultimately unable to obtain reliable values for expression (Fig. S4, *B* and *C*).

Although an inward-facing atorvastatin-bound structure of OATP1B1 could not be determined at high resolution, a lower-resolution reconstruction solved in this conformation in the absence of Sb5 is similar in conformation to the inward-facing structures reported to date, and a blob of density likely corresponding to atorvastatin, not visible in the apo structure, is present. Interestingly, the extra map density in the inward-facing conformation was observed near residues primarily on the C-lobe side of the pocket, consistent with observations of the outward-facing conformation (Figs. 2*D* and S5*B*). Its position is consistent with ligands in other substrate-bound structures and is similar to our outward-facing structure. As before, we used Autodock Vina predictions targeting the region surrounding this density to predict multiple distinct poses of similar confidence, with the acid moiety being positioned near the bottom or central portion of the major pocket or within the minor pocket. We conclude from these analyses that atorvastatin's interactions with the substrate-binding pocket are likely plastic, with multiple poses being accommodated by the largely hydrophobic pocket and several basic patches within the pocket providing favorable interactions for its acidic moiety. This broadly agrees with atorvastatin's role as an OATP1B1 substrate, for which protein-substrate interactions are necessarily transient and the protein must undergo significant conformational changes to transport substrates, resulting in remodeling of the pocket. It is also consistent with the broad substrate specificity of OATP1B1, providing favorable interactions for a wide variety of organic anionic substrates (19).

Cyclosporine A binding inhibits OATP1B1 by impeding its transition to the occluded conformation

Cyclosporine A, an immunosuppressant, is linked to a spectrum of DDIs rooted in its inhibition of OATP1B1-mediated transport (29), but unlike many other known OATP1B1 inhibitors, it is not also thought to be transported by OATP1B1. To illuminate the mechanism of OATP1B1 inhibition by cyclosporine A, we determined the structure of OATP1B1 in a complex with cyclosporine A and Sb5 (Fig. 3*A*). As before, although both inward- and outward-facing states were discernable in the dataset, the highest-resolution reconstruction captures the outward-facing conformation at 3.4 Å resolution. An oblong ring of density in the map is congruent both in size and shape with cyclosporine A residing in the major pocket (Fig. 3*A*, inset). Cyclosporine A was modeled into this density, although the lack of clear side chain density did not allow definitive identification of its specific interactions with the binding cavity. Its binding, however, appears to be primarily driven by interactions of the largely hydrophobic major pocket with the aliphatic side chains of cyclosporine A. In the absence of clear binary charged or polar interactions, the generic hydrophobicity of the large pocket could drive tight binding of cyclosporine A without strongly favoring the highly ordered conformation expected of an inhibitor, which would explain the absence of well-defined side chain density. Notably, in the presence of cyclosporine A, F356, which flanks the minor pocket, is displaced such that it protrudes into the minor pocket, acting as a gate to block access (Fig. 3*B*). This residue's conformation contrasts with that reported in other published structures, as well as the apo and atorvastatin-bound structures reported here, and its displacement appears to be a

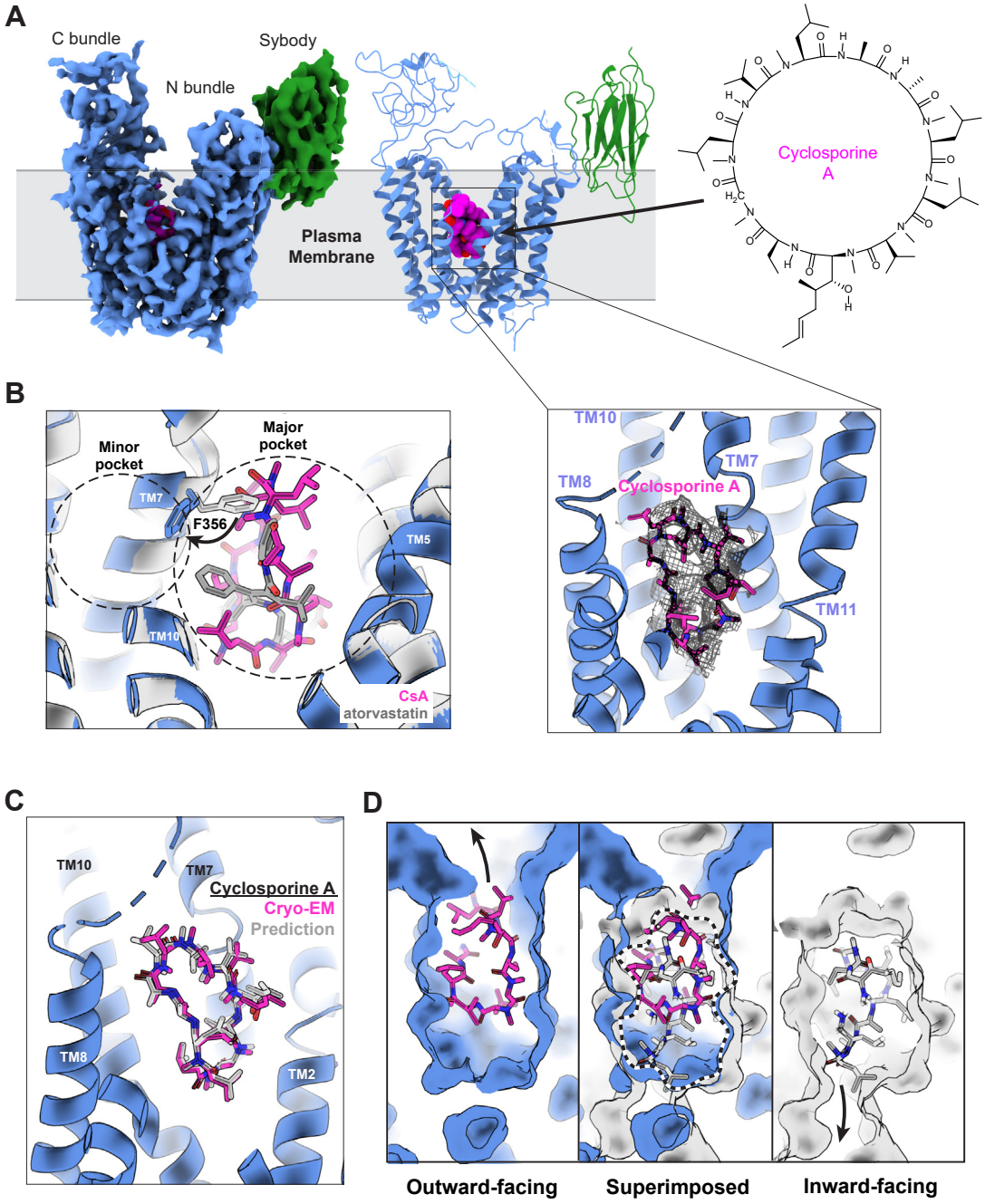

Figure 3. Structure of cyclosporine A-bound OATP1B1 with Sb5. *A*, cryo-EM map volume of outward-facing OATP1B1-Sb5 complex bound to cyclosporine A and ribbon representation of coordinates, colored by subunit, as indicated. The inset shows the cyclosporine A binding site with its corresponding map density, contoured at 3.0σ. *B*, structures of atorvastatin- and cyclosporine A-bound OATP1B1 are superimposed, with ligands shown in stick representation and colored as indicated, with major and minor pockets indicated by dotted circles. F356 is shown in stick representation, with its conformational change upon cyclosporine binding indicated by an *arrow*. *C*, the binding mode of cyclosporine A as built into the cryo-EM map (*green*) is superimposed with the top prediction from Autodock Vina (*magenta*). *D*, overlay of outward- and inward-facing structures of OATP1B1 suggest the transport pocket of the outward-occluded conformation is likely too small to accommodate cyclosporine A, preventing transport in either direction.

consequence of the bulk of cyclosporine A within the pocket, requiring its rearrangement to accommodate the ligand.

The overall conformation of OATP1B1-bound cyclosporine A is grossly similar to the many published cyclosporine A structures, with the ring collapsing on itself to form an oblong structure, but the local details of its conformation vary widely among known structures (30, 31). To better understand the potential for alternative cyclosporine A conformations and positions within the pocket, however, we again used the protein coordinates with Autodock Vina to predict possible binding modes. Remarkably, the top-scoring prediction overlays very closely (Fig. 3*C*) with the disposition of cyclosporine A in the cryo-EM structure, building confidence in this position and conformation.

Cyclosporine A binds stably and inhibits both the inward- and outward-facing conformations of OATP1B1, exhibiting a

slow off rate (k_{off}), but is not transported by OATP1B1 (32–34). When we measured its uptake by cells expressing OATP1B1 (*versus* wild-type/reference cells), a concentration- and time-dependent increase in intracellular cyclosporine A was observed, but OATP1B1 had no statistically significant impact on the uptake rate, suggesting that cyclosporine A can cross the plasma membrane passively, but is not transported as an OATP1B1 substrate (Fig. S5*A*). In contrast, rosuvastatin and atorvastatin, known as OATP1B1 transport substrates, exhibited significant uptake only when OATP1B1 was expressed. While we were unable to resolve both the outward- and inward-facing conformations of OATP1B1 at high resolution in the presence of cyclosporine A, low-resolution reconstructions of both forms, solved in the absence of Sb5, exhibit evidence of cyclosporine A density (Fig. S5*B*). Cyclosporine A occupies the major pocket in each of these conformations, but its position is shifted relative to the pocket in the inward-facing conformation, suggesting at least two possible binding modes, depending on the transporter conformation. Thus, we next examined whether steric effects might play a role in its inhibitory mechanism. While a high-resolution structure of OATP1B1 in its occluded state has not yet been reported, an approximation of the occluded pocket volume can be obtained through an overlay of the inward- and outward-facing structures (Figs. 3*D* and S6). A comparison of this pocket to the overall shape and volume of the bound cyclosporine A revealed that the pocket cannot easily accommodate it in the occluded conformation without significant steric clashes, which would explain the differences in the cyclosporine A binding mode in our inward- and outward-facing maps. More importantly, this analysis suggests that the transition of OATP1B1 from inward- or outward-facing states to the occluded state is made significantly less favorable by the presence of cyclosporine A, which is likely the basis of its inhibition.

Discussion

OATP1B1 is a hepatic transporter of the SLCO1 superfamily acting on a broad range of acidic transport substrates, including xenobiotics, which in some cases alter drug pharmacokinetics leading to DDIs. Statins, including the example discussed here, atorvastatin, use OATP1B1 as a major hepatic clearance route, and OATP1B1 inhibition by cyclosporine A and other drugs significantly alters their ADME properties. We have used cryo-EM to discover new insights into the structural basis of statin transport by OATP1B1, as well as the basis of its inhibition by cyclosporine A. Sb5, which was used to enable the high-resolution structures reported here, binds to the N-terminal extracellular domain of OATP1B1. The residues participating in this epitope are almost entirely conserved in OATP1B3 and thus may also find application as a tool for structural work on both transporters. Although Sb5 did not inhibit substrate transport by OATP1B1, and both inward- and outward-facing conformations were observed in our datasets, only the outward-facing conformation showed evidence of Sb5 binding and could be reconstructed at high resolution.

Dynamics between the inward- and outward-facing states of OATP1B1 are not yet fully understood, but it has been proposed that binding and release of bicarbonate on the extracellular and intracellular sides of the membrane, respectively, act as a critical switch to trigger these structural transitions. Based on our low-resolution Sb5-free reconstructions of OATP1B1 in both states and comparison to other published structures, free energy calculations suggest that each conformation has a similar stability (−28.0 kcal/mol IF and −27.2 kcal/mol OF) determined by its buried surface area (calculated using PISA (35)) encompassing contacts between the N and C lobes. This suggests that the transporter may sample both conformations freely at neutral pH and in the absence of other factors, which agrees with our observations.

While it was challenging to identify a strict binding pose for atorvastatin using density from the cryo-EM map, the ambiguity of its pose is likely consistent with its transport mechanism. Compared to other SLCs that transport organic ions, such as OATs and OCTs (24, 36, 37), OATP1B1 contains a larger internal cavity, allowing for a greater variety of potential binding interactions and a broader range of possible substrates. Given the need for a relatively loose association between the transporter and substrates, as opposed to the higher-affinity and more clearly defined interactions expected for an inhibitor, it is perhaps unsurprising that our binding pose predictions for the cavity yield widely differing results, some consistent with our interpretation of the atorvastatin-bound cryo-EM map and others appearing to agree with predictions made by others, but all satisfying key interactions for atorvastatin's hydrophobic and acidic moieties (19). While we were unable to reliably quantitate expression of OATP1B1 point mutants to normalize our transport assays, we nonetheless observed significant reductions in overall transport when individual surface-exposed residues forming the basic patch, including K41, K49, H555, and R580, were mutated to alanine. This hints that those residues may be important for interaction with the acidic moieties of transport substrates, though these unnormalized data must be interpreted with great caution. Taken together, the data suggest the overall orientation of transport substrates with their acidic regions oriented toward the basic patch and hydrophobic regions occupying the other side of the pocket but leaving significant room to interpret the specifics of the pose. Overall, our observations suggest that many OATP1B1 substrates may bind in any of multiple modes during transport.

Cyclosporine A, an inhibitor, but not a transport substrate, of OATP1B1, binds and inhibits both its inward- and outward-facing states. This is made possible by its ability to enter cells independently of OATP1B1, either through a different transporter or by passive diffusion, to accomplish *cis* or *trans* inhibition (32–34). Indeed, cyclosporine inhibition of OATP1B1 exhibits a time-dependent increase in inhibition in cells, consistent with a delay associated with the entry of cyclosporine through the plasma membrane to augment inhibition *in trans*. As we might expect, the conformation of cyclosporine A in our outward-facing cryo-EM structure appears somewhat more ordered and well-defined than that seen for atorvastatin,

consistent with its role as an inhibitor and suggesting a tighter interaction, probably driven in part by its ability to fill the transport cavity and participate in a greater variety of interactions with the transporter. Our structure suggests that the inhibitory mechanism of cyclosporine A is driven largely by its molecular bulk, which impedes the transition from inward- or outward-facing states to the intermediate occluded state by creating molecular clashes incompatible with the transition. Its overall ring-shaped structure likely contributes to a reduced flexibility that resists its accommodation in the pocket during this transition, which agrees with a comparison of the common cavity shared by our outward-facing structures with published inward-facing structures (19, 20). A combination of bulk and limited flexibility, as well as its lack of the acidic moieties present in most OATP1B1 substrates, may explain why cyclosporine A acts as an inhibitor of OATP1B1. Consistent with this hypothesis, rifampicin, which is smaller (weighing in at 823 Da) in size than cyclosporine A (which is 1203 Da) and better accommodated in this shared pocket volume, both inhibits and is transported by OATP1B1 (38), whereas the even smaller (585 Da) and more acidic bilirubin is a natural transport substrate, but does not inhibit transport.

Overall, we propose a model (Fig. 4) in which small acidic transport substrates, such as atorvastatin, find favorable interactions in the OATP1B1 pocket for their hydrophobic and acidic portions, with the large binding pocket supporting multiple binding modes compatible with transport. Transport occurs through free interconversion between the outward- and inward-facing states through an intermediate outward-occluded state, whose pocket is smaller in extent than that of the other two states. Interestingly, single-nucleotide polymorphisms (SNPs) in OATP1B1 associated with variations in patient responses to drugs map to locations distal to the ligand binding pocket, suggesting that they may act by exerting subtle effects on conformational changes required for transport, rather than by directly interacting with substrates (Fig. S9) (39–41). Cyclosporine A, which can bind both outward- and inward-facing states of OATP1B1 through hydrophobic interactions, acts as a plug in the major substrate pocket whose size is greater than that of the occluded state pocket and is thus incompatible with the transition through the occluded state to accomplish transport. While OATP1B1 transports a wide variety of substrates, the insights provided by these atorvastatin- and cyclosporine A-bound structures offer clues to more general principles underlying OATP1B1 transport and inhibition, shedding light on a target that lies at the center of many clinically important DDIs and offering new potential avenues for improvements in drug design.

Experimental procedures

Reagents and cell lines

The open reading frame DNA sequence of human OATP1B1 (UniProt ID Q9Y6L6-1) corresponding to D2-C691 was synthesized and codon-optimized for insect cell expression by GenScript with an N-terminal FLAG tag followed by a GSS linker and a C-terminal GSSS linker followed by a BAP tag in pFastBac (Thermo Fisher). The insert was also subcloned into pcDNA3.1(+) (Thermo Fisher) for expression in mammalian cells. Additional constructs were synthesized to further investigate key interactions. These included a full-length, wild-type OATP1B1 construct as well as constructs which each contain a single point mutant: K41A, K49A, R580A, H555A, H555F, and R633A all subcloned into pcDNA3.1(+). Reagents for the Expi293 expression system and Opti-MEM were obtained from ThermoFisher. Rosuvastatin was purchased from Biosynth. Cyclosporine A, atorvastatin, and rifamycin SV were purchased from Sigma-Aldrich, Inc. BioCoat 96-well poly-D-lysine 96-well plates and HEPES (4-(2-Hydroxyethyl) piperazine-1-ethanesulfonic acid) were obtained from Corning Inc. DMEM (Dulbecco's Modified Eagle Medium), HBSS (Hank's Balanced Salt Solution), gentamicin, NEAA, GlutaMax, and sodium pyruvate were obtained from Gibco Life Technologies. HEK293-WT cells were from Pfizer (Sandwich, UK), and HEK293-OATP1B1 cells were from Pfizer. Sb5 was generated by Linkster Therapeutics AG.

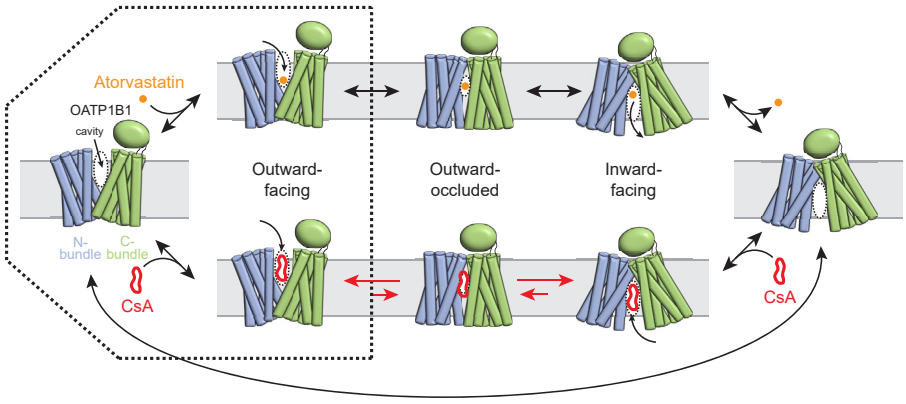

Figure 4. A model for OATP1B1 statin transport and inhibition by cyclosporine A. Cartoon representation of the OATP1B1 transport cycle and the impacts of atorvastatin and cyclosporine A. In the outward-facing and inward-facing conformations of OATP1B1, the ligand-binding cavity of OATP1B1 is sufficiently large to accommodate atorvastatin or CsA. For atorvastatin, the transition through the outward-occluded state with its reduced-volume cavity, to the inward-open state completes transport across the membrane. Binding of CsA, which can occur to either the outward-open or inward-open state of OATP1B1, does not allow transport because the transition to the outward-occluded state is highly unfavorable, as the smaller cavity of this state is too small to accommodate CsA. Thus, CsA acts as an inhibitor, but not a substrate, of OATP1B1.

In vitro *studies in cells*

Cell preparation for transport studies

For OATP1B1 substrate/inhibition transport assays, wild-type HEK293 and stably transfected cells expressing OATP1B1 were thawed and seeded in DMEM high glucose (supplemented with 10% fetal bovine serum, 1% 10 mg/ml gentamicin, 1% 100× NEAA, 1% 100× GlutaMAX, and 1% 100 mM sodium pyruvate) at a density of 5 to 7.5 × 10^4 cells/well on BioCoat 96-well poly-D-lysine coated plates and cultured for 3 days. Cells were maintained at 37 °C, 5% CO_2, and 90% relative humidity.

For transport assays with OATP1B1 point mutants, wild-type and mutant Expi293 expression for the mutant transporter studies was performed using the Expi293 system as per protocol. The cells were grown in suspension in shake flasks containing Expi293 medium at 37C, 125 rpm, and 8% CO2 for 24 h. The cells were then enhanced, as per the Expi293 system protocol, and allowed to shake for 5 more hours after which they were then quantitated, and cells were plated onto two replicate 96 well poly-D-lysine coated plates. The wild-type OATP1B1 construct was plated at 100K cells per well in 200 µL. The mutants were plated at 200K cells per well in 200 µL. The cells were then grown in a stationary incubator at 37C and 8% CO2 for 20 h. The cells were then used for transport studies.

Transport studies

Transport buffer was prepared at pH 7.4 using HBSS supplemented with 20 mM HEPES. Stock solutions of all compounds were diluted in a transport buffer. All cell plates were washed three times with transport buffer and pre-incubated for 2 to 5 min with blank transport buffer at 37 °C.

To assess the transporter-mediated uptake of atorvastatin and cyclosporine A, the HEK-WT and HEK-OATP1B1 cells were incubated with 0.05 ml of atorvastatin, cyclosporine A, and rosuvastatin (positive control) on a heated shaker at 37 °C at multiple time points. The uptake assays were stopped by the removal of the dosing solution followed by three quick washes with ice-cold HBSS.

To assess the transporter-mediated uptake of rosuvastatin and atorvastatin, the HEK-WT, HEK-OATP1B1 (WT), and the five OATP1B1 mutant cells were incubated with 0.05 ml of rosuvastatin and atorvastatin on a heated shaker at 37 °C for 1-min timepoint. The uptake assays were stopped by the removal of the dosing solution followed by three quick washes with ice-cold HBSS.

To assess the transporter-mediated inhibitory potency of atorvastatin, cyclosporine A, and Sb5, the HEK-OATP1B1 cells were preincubated with 0.05 ml of the test inhibitors or control inhibitor (rifamycin SV) for 30 min at 37 °C, 5% CO_2, and 90% relative humidity. The inhibition assay was initiated by the removal of the preincubation buffer and the addition of the probe substrate (rosuvastatin or atorvastatin) and the test compounds or control inhibitor on a heated shaker at 37 °C, for 1- or 2-min timepoints, respectively. Assay plates were stopped by the removal of the dosing solution followed by three quick washes with ice-cold HBSS.

Intracellular accumulation of atorvastatin, cyclosporine A, and rosuvastatin were extracted with 0.23 ml/well of 100% methanol containing internal standard. Cells were shaken for 30 to 60 min at room temperature. Cell extracts were transferred to 96-well plates, centrifuged, and 0.2 ml/well was transferred to new 96-well plates and dried down under nitrogen. Samples were reconstituted with 50:50 methanol:water and analyzed by tandem liquid chromatography-mass spectrometry (LC-MS/MS).

Total cell protein per well per cell type was determined using a bicinchoninic acid protein assay for the substrate assay (Pierce, Thermo Fisher Scientific), following the manufacturer's recommended protocol.

Add expression-level quantitation method

LC-MS/MS analysis of In vitro *samples*

In vitro samples were received dried down and reconstituted in 100 µl of 50:50 methanol: water. Samples were then vortexed, spun, and analyzed by LC-MS/MS using a Sciex Triple Quad 6500+ mass spectrometer (Sciex), equipped with an electrospray source, an Agilent 1290 Infinity II binary pump (Agilent) and a PAL system RSI 850 autosampler (CTC Analytics). Chromatographic separation for atorvastatin and rosuvastatin was achieved using a Waters Acquity UPLC HSS T3 column (1.8 µm, 2.1 × 50 mm), and for cyclosporine A, Phenomenex Kinetics C18 column (2.6 µm, 2.1 × 30 mm), both maintained at 60 °C with a flow rate of 0.8 ml/min. The mobile phase (2 solvents, gradient) was optimized to achieve good separation between the analytes. Solvent A was water containing 0.1% formic acid, and solvent B was acetonitrile containing 0.1% formic acid. The gradient for atorvastatin and rosuvastatin began at 5% B until 0.1 min, followed by an increase to 95% B at 0.5 min, held until 0.70 min, then decreased back to 5% B at 0.75 min, maintaining initial conditions from 0.75 to 2 min. The gradient for cyclosporine A began at 30% B until 0.1 min, followed by an increase to 95% B at 0.3 min, held until 0.70 min, then decreased back to 30% B at 0.75 min, maintaining initial conditions from 0.75 to 1.5 min. LC-MS/MS methods for the different analytes analyzed are presented in Table S2. Analyst 1.7 software was used for peak integration (area ratios).

Expression and purification of OATP1B1 for structural studies and sybody generation

Mammalian cell expression was performed using the Expi293 system from Thermo Fisher. Cells were transfected with 1 mg/L of endotoxin-free plasmid DNA for 48 h, at which point they were collected by centrifugation and stored at −80. For biotinylated protein, the cells were co-transfected with 0.4 mg/L of a plasmid expressing BirA (UniProt ID P06709) and D-biotin was added to the media at 50 µM final concentration.

Cells were resuspended in 50 ml buffer containing 25 mM HEPES pH 7.5, 200 mM NaCl, protease inhibitor cocktail, and lysed by Dounce Homogenizer. Cell lysate was centrifuged at 40,000 rpm for 25 min at 4 °C to remove cell debris. The

pelleted membrane fraction was resuspended and solubilized in 25 mM HEPES pH 7.5, 150 mM NaCl, 1% LMNG (w/v), 0.2% CHS (w/v) for at 4 °C for 2 h, and centrifuged at 40, 000 rpm for 25 min at 4 °C to pellet insoluble debris. Supernatant was loaded to Talon affinity resin and washed in buffer containing 25 mM HEPES pH 7.5, 150 mM NaCl, 0.01% LMNG (w/v), 0.002% CHS (w/v), and eluted with buffer containing 25 mM HEPES pH 7.5, 150 mM NaCl, 0.01% LMNG (w/v), 0.002% CHS (w/v) and 200 mM Imidazole. Eluted fractions were pooled and concentrated for further purification by size-exclusion chromatography (SEC) on a Superose 6 10/300 Gl column (GE Healthcare) in the above wash buffer. This purification strategy revealed monodisperse behavior consistent with the monomeric size of the protein. Assessment of protein purity and quality was further performed using SDS-PAGE. Notably, smearing protein bands near 80 kDa were observed, indicating proper glycosylation as expected (Fig. S7). Biotinylated OATP1B1 was also purified in the same scheme showing a monodisperse profile from SEC, and further assessed by SDS-PAGE. SDS-PAGE gels were imaged using a Bio-Rad GelDoc EZ Imager with Image Lab 6.1 software.

Sybody generation against OATP1B1

Sybody molecules were selected as described previously (21, 42) against purified C-terminally biotinylated human OATP1B1 (SLCO1B1) transporter protein in the presence of 10 μM cyclosporine A (Merck, cat. no. 30024). Individual clones were expressed in *E. coli* MC1061, extracted from the cells by periplasmic extraction, and analyzed for binding against human OATP1B1 protein (purified from Expi293 cells as described above) in the presence and absence of cyclosporine A by enzyme-linked immunosorbent assay (ELISA). Positive hits were purified using immobilized metal affinity chromatography (IMAC) and SEC in TBS pH 7.5. Grating-coupled interferometry (GCI) measurements were made using a Creoptix WAVE system against OATP1B1 immobilized on a streptavidin-coated WAVEchip 4PCP-STA (Creoptix).

Affinity determination of Sb5 against OATP1B1

Affinities were determined by grating-coupled interferometry (GCI) measurements using a Creoptix WAVE system. Biotinylated OATP1B1 was immobilized on a streptavidin-coated 4PCP-STA WAVEchip (Creoptix) to a density of 1400 to 1600 pg/mm^2. Binding kinetics were measured at 25 °C in 25 mM Tris pH7.5, 300 mM NaCl, 0.01% LMNG, 0.002% CHS running buffer. Sb_05 was injected at 4 different concentrations (3, 9, 27, and 81 nM) using a flow rate of 30 μl/min for 240 s, and dissociation was probed for 600 s. The sensorgrams were fitted with the Creoptix software using double-referencing and fitted using a 1:1 model.

Cryo-EM sample preparation

Proteins were concentrated to 10 μM and used directly for cryo-EM for apo. Cyclosporine A at the final concentration of 30 μM from 30 mM stock in DMSO was added to OATP1B1. For Sb5 bound OATP1B1 proteins, OATP1B1 was incubated with 20 μM Sb5, and subsequently cyclosporine A and atorvastatin at the final concentration of 30 μM and 0.1% β-OG were added and incubated for 10 min on ice, respectively. 4 μl of proteins from each sample were applied to a flow-discharged Quantifoil R2/1200-mesh gold holey carbon grid and blotted for 3 s with blotting force 3 at 4 °C and 100% humidity. The grids were flash-frozen in liquid ethane cooled by liquid nitrogen with Vitrobot (Mark IV, Thermo Fisher Scientific).

Cryo-EM data collection, processing, and analysis

Grids were imaged utilizing a Titan Krios G2 transmission electron microscope operated at 300 kV, equipped with a Falcon 4i direct electron detector and Selectris X imaging filter. All screening and data collection procedures were executed in EPU (Thermo Fisher Scientific) in counting mode.

Data processing pipelines for samples containing OATP1B1 apo, OATP1B1 + cyclosporine A, OATP1B1 + atorvastatin, OATP1B1 + Sb5, OATP1B1 + Sb5 + cyclosporine A, and OATP1B1 + Sb5 + Atorvastatin are detailed in the supporting information (Figs. S9–S14). EER format movies were recorded at a nominal magnification of 1,650,00x (pixel size of 0.733 Å). Each micrograph was dose-fractionated to 65 frames with a total dose of ∼60 e/A^2, and the defocus range was set from −0.6 μm to −2.2 μm. Motion correction and CTF estimation were performed using MotionCor2 (43) and CTFFIND4.1 (44–46) For OATP1B1 + Sb5, particles were initially auto-picked using the Blob Picker feature in CryoSPARC from the first 3000 micrographs. These particles underwent three rounds of 2D classification to generate 2D references of OATP1B1 + Sb5 data sets for the CryoSPARC template picker. For all OATP1B1 datasets, particles were picked from the entire micrographs using both blob- and template pickers. Duplicates from merged particles were removed (0.5 separation dist), yielding particles as shown in Table S1. Initial particle extraction involved binning by 4 to a box size of 360 pixels (pixel size of 4.40 Å/pixel) for expedited data processing. Additional rounds of 2D classifications with gradually increasing *initial classification uncertainty factor* (2–10) were performed to identify high-resolution particles revealing secondary structure features. Due to the robust preferred orientation, particles were balanced through the mitigation of dominant views after 2D classification as indicated in the workflow.

A subset of particles from good 2D class averages was used for *ab initio* model generation in CryoSPARC, subsequently employed in multiple rounds of heterogeneous refinement and further 2D classification to filter out poor-quality particles. Characterizing sybody-free OATP1B1 conformations poses a formidable challenge. Remarkably, a 3D Variability Analysis of the particles at the last step unveiled dynamic conformational changes akin to a transition from the inward-facing to outward-facing conformations. Employing extreme conformations from this spectrum in IF-OF facilitated Heterogenous refinement allowed for enabled efficient classifications (Fig. S13).

The yielded particles were re-extracted to 1.1 Å/pixel and used for non-uniform refinement and local refinement. For select datasets, the final particles were exported to RELION 4.0 (25) for focused 3D classification. 3D classifications without alignment were conducted with the regularization factor indicated in Table S1. Particles from the best classes were imported back into CryoSPARC and subjected to non-uniform refinement, local refinement, and local CTF refinement, as described in Figures S10–S15. The high-resolution final maps with Sb5 underwent map modification implemented in PHENIX using two independent half maps and the corresponding mask as input. For the low-resolution, poor-quality final maps of OATP1B1 without Sb5, DeepEMhancer was employed for post-processing.

Atomic models of full-length OATP1B1 and Sb5 were predicted using AlphaFold (47) and subsequently rigid-body fitted into the cryo-EM maps. To improve the model quality, residues in the loop regions, and side chains with weak densities were removed. The model was then iteratively built into the map using Coot (v0.9.8.) (48) in conjunction with real-space refinement in PHENIX (49). This iterative process resulted in the production of the final refined model. The complete cryo-EM data processing workflow, as well as the validation metrics, and the statistics pertaining to the model refinement (refer to Table S1), can be found in the supporting information. Figures based on the final structure were generated using PyMol version 2.5.4, UCSF Chimera version 1.16 (50), and ChimeraX version 1.4 (51). 3D variability analysis (3DVA) was performed (52), and the results were reconstructed at 6 Å filtered resolution and shown at 6.1σ.

Ligand docking

AutoDock Vina was executed utilizing the PyMOL plugin DockingPie 1.0.1 (25, 26, 53) to perform molecular docking simulations involving Cyclosporin A and Atorvastatin in both intracellular (IF) and extracellular (OF) conformations. The organic anion transporter (OAT) served as the receptor, with Atv or CsA acting as ligands. The grid space parameters, specified in Angstrom, were as follows: Grid center coordinates X 130.36 Y 132.19 Z 126.0 OATP1B1-Sb5-OF-Cyclosporine A, Grid center coordinates X 132.00 Y 140.74 Z 131.87 OATP1B1-IF-Cyclosporine A, Grid center coordinates X 131.2 Y 134.18 Z 139.02 OATP1B1-Sb5-OF-Atorvastatin, Grid center coordinates X 130.39 Y 139.45 Z 131.84 OATP1B1-IF- Atorvastatin. And Grid dimensions X 24 Y 28 Z 24 for all the dockings. Exhaustiveness was consistently set at 20, Energy Range at 3, and Poses at 20. Evaluation of the *in silico* dockings relied on affinity scores (in kcal/mol) and alignment with the cryo-EM map. AutoDock Vina generated PDBQT output files, subsequently visualized in PyMOL.

Data availability

The cryo-EM maps generated in this study have been deposited in the Electron Microscopy Data Bank under accession codes EMD-46004 (outward-facing apo-OATP1B1 with Sb5), EMD-46006 (outward-facing OATP1B1 with Sb5 and cyclosporine A), EMD-46005 (outward-facing OATP1B1 with Sb5 and atorvastatin), EMD-46413 (inward-facing sybody-free apo-OATP1B1), EMD-46414 (outward-facing sybody-free apo-OATP1B1), EMD-46411 (inward-facing sybody-free OATP1B1 with cyclosporine A), EMD-46412 (outward-facing sybody-free OATP1B1 with cyclosporine A), EMD-46407 (inward-facing sybody-free OATP1B1 with atorvastatin), EMD-46408 (outward-facing sybody-free OATP1B1 with atorvastatin). The atomic coordinates corresponding to the cryo-EM maps generated in this study have been deposited in the Protein Data Bank under accession codes 9CY1 (outward-facing apo-OATP1B1 with Sb5), 9CY4 (outward-facing OATP1B1 with Sb5 and cyclosporine A), and 9CY3 (outward-facing OATP1B1 with Sb5 and atorvastatin). Source data are provided with this paper.

Supporting information—This article contains supporting information.

Acknowledgments—The authors gratefully acknowledge Steve Gernhardt, Larisa Zueva, and Jamie Tourville for mass spectrometry analyses, and Dr Manthena Varma for critical reading of the manuscript.

Author contributions—I. Z., R. J. P. D., C. C., A. D. R., S. L., S. H., M. W. S., J. A. L., and K. F. F. writing–review & editing; I. Z., R. J. P. D., A. D. R., S. L., S. H., M. W. S., and J. A. L. validation; I. Z., R. J. P. D., S. L., and S. H. project administration; I. Z., R. J. P. D., C. C., A. D. R., K. H., L. M. H., S. L., S. H., M. W. S., K. F. F., M. W., and J. A. L. methodology; I. Z., R. J. P. D., C. C., A. D. R., K. H., L. M. H., S. L., S. H., M. W. S., K. F. F., M. W., and J. A. L. conceptualization; C. C., S. L., S. H., M. W. S., and M. W. visualization; C. C., K. H., L. M. H., and M. W. S. investigation; K. H., L. M. H., S. L., M. W. S., and M. W. formal analysis; S. L. and S. H. supervision.

Funding and additional information—All work described in this manuscript was funded by Pfizer, Inc. and Linkster Therapeutics.

Conflict of interest—The authors declare the following financial interests/personal relationships which may be considered as potential competing interests: M. W. S., K. H., J. A. L., K. F. F., M. A. W., C. C., A. D. R., S. L., and S. H. were employees of Pfizer, Inc at the time this work was performed and may hold Pfizer stock. I. Z., R. J. P. D. and L. M. H. are employees of Linkster Therapeutics AG and may be Linkster shareholders.

Abbreviations—The abbreviations used are: ADME, absorption, distribution, metabolism, and elimination; cryo-EM, Cryo-electron microscopy; DCF, 2′7′-dichlorofluorescein; DDIs, drug-drug interactions; EMA, European Medical Agency; FDA, United States Food and Drug Administration; MFS, major facilitator subfamily; OAT, organic anion transporter; OATP, organic anion transporter polypeptides; OCT, organic cation transporter.

References

1. Svoboda, M., Riha, J., Wlcek, K., Jaeger, W., and Thalhammer, T. (2011) Organic anion transporting polypeptides (OATPs): regulation of expression and function. *Curr. Drug Metab.* **12**, 139–153
2. Hagenbuch, B., and Meier, P. J. (2004) Organic anion transporting polypeptides of the OATP/SLC21 family: phylogenetic classification as

OATP/SLCO superfamily, new nomenclature and molecular/functional properties. *Pflugers Arch.* **447**, 653–665
3. Kullak-Ublick, G. A., Beuers, U., Meier, P. J., Domdey, H., and Paumgartner, G. (1996) Assignment of the human organic anion transporting polypeptide (OATP) gene to chromosome 12p12 by fluorescence in situ hybridization. *J. Hepatol.* **25**, 985–987
4. Obaidat, A., Roth, M., and Hagenbuch, B. (2012) The expression and function of organic anion transporting polypeptides in normal tissues and in cancer. *Annu. Rev. Pharmacol.* **52**, 135–151
5. Smith, N. F., Figg, W. D., and Sparreboom, A. (2005) Role of the liver-specific transporters OATP1B1 and OATP1B3 in governing drug elimination. *Expert Opin. Drug Metab. Toxicol.* **1**, 429–445
6. Roth, M., Obaidat, A., and Hagenbuch, B. (2012) OATPs, OATs and OCTs: the organic anion and cation transporters of the SLCO and SLC22A gene superfamilies. *Br. J Pharmacol* **165**, 1260–1287
7. Nigam, A. K., Momper, J. D., Ojha, A. A., and Nigam, S. K. (2024) Distinguishing molecular properties of OAT, OATP, and MRP drug substrates by machine learning. *Pharmaceutics* **16**, 592
8. Abe, T., Kakyo, M., Tokui, T., Nakagomi, R., Nishio, T., Nakai, D., *et al.* (1999) Identification of a novel gene family encoding human liver-specific organic anion transporter LST-1. *J. Biol. Chem.* **274**, 17159–17163
9. Konig, J., Cui, Y., Nies, A. T., and Keppler, D. (2000) A novel human organic anion transporting polypeptide localized to the basolateral hepatocyte membrane. *Am. J. Physiol. Gastrointest. Liver Physiol.* **278**, G156–G164
10. Konig, J., Cui, Y., Nies, A. T., and Keppler, D. (2000) Localization and genomic organization of a new hepatocellular organic anion transporting polypeptide. *J. Biol. Chem.* **275**, 23161–23168
11. Abe, T., Unno, M., Onogawa, T., Tokui, T., Kondo, T. N., Nakagomi, R., *et al.* (2001) LST-2, a human liver-specific organic anion transporter, determines methotrexate sensitivity in gastrointestinal cancers. *Gastroenterology* **120**, 1689–1699
12. EMA (2024) *ICH Guideline M12 on Drug Interaction Studies*, European Medicines Agency, Amsterdam, the Netherlands
13. FDA (2024) *M12 Drug Interaction Studies: Guidance for Industry*. Food and Drug Administration, Rockville, MD
14. Kellick, K. A., Bottorff, M., Toth, P. P., and The National Lipid Association's Safety Task, F. (2014) A clinician's guide to statin drug-drug interactions. *J. Clin. Lipidol.* **8**, S30–S46
15. Billington, S., Shoner, S., Lee, S., Clark-Snustad, K., Pennington, M., Lewis, D., *et al.* (2019) Positron emission tomography imaging of [C] rosuvastatin hepatic concentrations and hepatobiliary transport in humans in the absence and presence of Cyclosporin A. *Clin. Pharmacol. Ther.* **106**, 1056–1066
16. Åsberg, A., Hartmann, A., Fjeldså, E., Bergan, S., and Holdaas, H. (2001) Bilateral pharmacokinetic interaction between cyclosporine A and atorvastatin in renal transplant recipients. *Am. J. Transpl.* **1**, 382–386
17. Omar, M. A., Wilson, J. P., and Cox, T. S. (2001) Rhabdomyolysis and HMG-CoA reductase inhibitors. *Ann. Pharmacother.* **35**, 1096–1107
18. Lees, J. A., and Han, S. (2022) Cryo-EM and SLC transporters. In *2022 Medicinal Chemistry Reviews*, American Chemical Society, Washington, DC: 489–512
19. Ciuta, A. D., Nosol, K., Kowal, J., Mukherjee, S., Ramírez, A. S., Stieger, B., *et al.* (2023) Structure of human drug transporters OATP1B1 and OATP1B3. *Nat. Commun.* **14**, 5774
20. Shan, Z. Y., Yang, X. M., Liu, H. H., Yuan, Y. F., Xiao, Y., Nan, J., *et al.* (2023) Cryo-EM structures of human organic anion transporting polypeptide OATP1B1. *Cell Res.* **33**, 940–951
21. Zimmermann, I., Egloff, P., Hutter, C. A. J., Arnold, F. M., Stohler, P., Bocquet, N., *et al.* (2018) Synthetic single domain antibodies for the conformational trapping of membrane proteins. *Elife* **7**, e34317
22. Leuthold, S., Hagenbuch, B., Mohebbi, N., Wagner, C. A., Meier, P. J., and Stieger, B. (2009) Mechanisms of pH-gradient driven transport mediated by organic anion polypeptide transporters. *Am. J. Physiol. Cell Physiol.* **296**, C570–C582
23. Weaver, Y. M., and Hagenbuch, B. (2010) Several conserved positively charged amino acids in OATP1B1 are involved in binding or translocation of different substrates. *J. Membr. Biol.* **236**, 279–290
24. Khanppnavar, B., Maier, J., Herborg, F., Gradisch, R., Lazzarin, E., Luethi, D., *et al.* (2022) Structural basis of organic cation transporter-3 inhibition. *Nat. Commun.* **13**, 6714
25. Eberhardt, J., Santos-Martins, D., Tillack, A. F., and Forli, S. (2021) AutoDock Vina 1.2.0: new docking methods, expanded force field, and Python bindings. *J. Chem. Inf. Model.* **61**, 3891–3898
26. Trott, O., and Olson, A. J. (2010) Software news and update AutoDock Vina: improving the speed and accuracy of docking with a new scoring function, efficient optimization, and multithreading. *J. Comput. Chem.* **31**, 455–461
27. Yue, M., Yang, J. J., Jin, M., Steier, B., Xiang, Y. Q., Zhang, H. J., *et al.* (2019) Gly45 and Phe555 in transmembrane domains 1 and 10 are critical for the activation of organic anion transporting polypeptide 1B3 by epigallocatechin gallate. *J. Agric. Food Chem* **67**, 9079–9087
28. DeGorter, M. K., Ho, R. H., Leake, B. F., Tirona, R. G., and Kim, R. B. (2012) Interaction of three regiospecific amino acid residues is required for OATP1B1 gain of OATP1B3 substrate specificity. *Mol. Pharmaceut.* **9**, 986–995
29. Neuvonen, P. J., Niemi, M., and Backman, J. T. (2006) Drug interactions with lipid-lowering drugs: mechanisms and clinical relevance. *Clin. Pharmacol. Ther.* **80**, 565–581
30. Corbett, K. M., Ford, L., Warren, D. B., Pouton, C. W., and Chalmers, D. K. (2021) Cyclosporin structure and permeability: from A to Z and beyond. *J. Med. Chem.* **64**, 13131–13151
31. Witek, J., Keller, B. G., Blatter, M., Meissner, A., Wagner, T., and Riniker, S. (2016) Kinetic models of Cyclosporin A in polar and apolar environments reveal multiple congruent conformational states. *J. Chem. Inf. Model.* **56**, 1547–1562
32. Izumi, S., Nozaki, Y., Lee, W., and Sugiyama, Y. (2022) Experimental and modeling evidence supporting the -inhibition mechanism for preincubation time-dependent, long-lasting inhibition of organic anion transporting polypeptide 1B1 by cyclosporine A. *Drug Metab. Disposition* **50**, 541–551
33. Nozaki, Y., and Izumi, S. (2023) Preincubation time-dependent, long-lasting inhibition of drug transporters and impact on the prediction of drug-drug interactions. *Drug Metab. Disposition* **51**, 1077–1088
34. Shitara, Y., Takeuchi, K., Nagamatsu, Y., Wada, S., Sugiyama, Y., and Horie, T. (2012) Long-lasting inhibitory effects of Cyclosporin A, but not tacrolimus, on OATP1B1-and OATP1B3-mediated uptake. *Drug Metab. Pharmacok* **27**, 368–378
35. Krissinel, E., and Henrick, K. (2007) Inference of macromolecular assemblies from crystalline state. *J. Mol. Biol.* **372**, 774–797
36. Dou, T. Y., Lian, T. F., Shu, S., He, Y., and Jiang, J. S. (2023) The substrate and inhibitor binding mechanism of polyspecific transporter OAT1 revealed by high-resolution cryo-EM. *Nat. Struct. Mol. Biol.* **30**, 1794–1805
37. Parker, J. L., Kato, T., Kuteyi, G., Sitsel, O., and Newstead, S. (2023) Molecular basis for selective uptake and elimination of organic anions in the kidney by OAT1. *Nat. Struct. Mol. Biol.* **30**, 1786–1793
38. International Transporter, C., Giacomini, K. M., Huang, S. M., Tweedie, D. J., Benet, L. Z., Brouwer, K. L., *et al.* (2010) Membrane transporters in drug development. *Nat. Rev. Drug Discov.* **9**, 215–236
39. Choudhuri, S., and Klaassen, C. D. (2020) Elucidation of OATP1B1 and 1B3 transporter function using transgenic rodent models and commonly known single nucleotide polymorphisms. *Toxicol. Appl. Pharmacol.* **399**, 115039
40. Kalliokoski, A., and Niemi, M. (2009) Impact of OATP transporters on pharmacokinetics. *Br. J. Pharmacol.* **158**, 693–705
41. Anabtawi, N., Drabison, T., Hu, S., Sparreboom, A., and Talebi, Z. (2022) The role of OATP1B1 and OATP1B3 transporter polymorphisms in drug disposition and response to anticancer drugs: a review of the recent literature. *Expert Opin. Drug Metab. Toxicol.* **18**, 459–468
42. Zimmermann, I., Egloff, P., Hutter, C. A. J., Kuhn, B. T., Brauer, P., Newstead, S., *et al.* (2020) Generation of synthetic nanobodies against delicate proteins. *Nat. Protoc.* **15**, 1707–1741
43. Zheng, S. Q., Palovcak, E., Armache, J. P., Verba, K. A., Cheng, Y. F., and Agard, D. A. (2017) MotionCor2: anisotropic correction of beam-induced

motion for improved cryo-electron microscopy. *Nat. Methods* **14**, 331–332
44. Rohou, A., and Grigorieff, N. (2015) CTFFIND4: fast and accurate defocus estimation from electron micrographs. *J. Struct. Biol.* **192**, 216–221
45. Punjani, A., Rubinstein, J. L., Fleet, D. J., and Brubaker, M. A. (2017) cryoSPARC: algorithms for rapid unsupervised cryo-EM structure determination. *Nat. Methods* **14**, 290–296
46. Scheres, S. H. W. (2012) RELION: implementation of a Bayesian approach to cryo-EM structure determination. *J. Struct. Biol.* **180**, 519–530
47. Jumper, J., and Hassabis, D. (2022) Protein structure predictions to atomic accuracy with AlphaFold. *Nat. Methods* **19**, 11–12
48. Emsley, P., Lohkamp, B., Scott, W. G., and Cowtan, K. (2010) Features and development of. *Acta Crystallogr. D* **66**, 486–501
49. Liebschner, D., Afonine, P. V., Baker, M. L., Bunkóczi, G., Chen, V. B., Croll, T. I., *et al.* (2019) Macromolecular structure determination using X-rays, neutrons and electrons: recent developments in. *Acta Crystallogr. Sect. D Struct. Biol.* **75**, 861–877
50. Pettersen, E. F., Goddard, T. D., Huang, C. C., Couch, G. S., Greenblatt, D. M., Meng, E. C., *et al.* (2004) UCSF chimera - a visualization system for exploratory research and analysis. *J. Comput. Chem.* **25**, 1605–1612
51. Pettersen, E. F., Goddard, T. D., Huang, C. R. C., Meng, E. E. C., Couch, G. S., Croll, T. I., *et al.* (2021) UCSF ChimeraX: structure visualization for researchers, educators, and developers. *Protein Sci.* **30**, 70–82
52. Punjani, A., and Fleet, D. J. (2021) 3D variability analysis: resolving continuous flexibility and discrete heterogeneity from single particle cryo-EM. *J. Struct. Biol.* **213**, 107702
53. Rosignoli, S., and Paiardini, A. (2022) DockingPie: a consensus docking plugin for PyMOL. *Bioinformatics* **38**, 4233–4234